



Simultaneous multislice diffusion-weighted imaging in whole-body positron emission tomography/magnetic resonance imaging for multiparametric examination in oncological patients

Jana Taron¹ · Christina Schraml¹ · Christina Pfannenbergl¹ · Matthias Reimold³ · Nina Schwenzer² · Konstantin Nikolaou¹ · Petros Martirosian² · Ferdinand Seith¹

Received: 23 March 2017 / Revised: 16 November 2017 / Accepted: 27 November 2017 / Published online: 26 February 2018

© European Society of Radiology 2018

Abstract

Objectives The aim of this study was to compare the diagnostic performance of simultaneous multislice diffusion-weighted imaging (DWI-SMS) with that of standard DWI (DWI-STD) in whole-body 3-T PET/MRI examination protocols in oncological patients.

Methods In a phantom study, we evaluated the apparent diffusion coefficients (ADC) from the two techniques. In ten volunteers, we assessed ADC values in different organs. In 20 oncological patients, we evaluated subjective image quality (Likert scale, 5 indicating excellent) and artefacts in different body regions. We also rated the conspicuity and acquired the ADC values of PET-positive tumorous lesions.

Results The scan time for the whole-body DWI-SMS examinations was 40% shorter than the scan time for the DWI-STD examinations (84 s vs. 140 s per table position). The phantom and volunteer studies showed lower ADC values from DWI-SMS in the liver and muscle (psoas muscle 1.4 vs. 1.3). In patients, DWI-SMS provided poorer subjective image quality in the thoracoabdominal region (3.0 vs. 3.8, $p = 0.02$) and overall more artefacts (138 vs. 105). No significant differences regarding conspicuity and ADC values of lesions were found.

Conclusions DWI-SMS seems to provide reliable conspicuity and ADC values of tumorous lesions similar to those provided by DWI-STD. Therefore, although providing poorer image quality in certain regions, DWI-SMS can clearly reduce PET/MRI scan times in oncological patients.

Key points

- DWI-SMS can reduce PET/MRI scan times in oncological patients.
- DWI-SMS provides reliable ADC values and good lesion conspicuity similar to those provided by DWI-STD.
- DWI-SMS may provide poorer image quality in regions with low signal.

Keywords Diffusion-weighted imaging · Whole-body · Oncology · Positron emission tomography · Multiparametric

✉ Petros Martirosian
petros.martirosian@med.uni-tuebingen.de

¹ Diagnostic and Interventional Radiology, University Department of Radiology, University Hospital of Tuebingen, Hoppe-Seyler-Str. 3, 72076 Tuebingen, Germany

² Section on Experimental Radiology, Diagnostic and Interventional Radiology, University Department of Radiology, University Hospital of Tuebingen, Hoppe-Seyler-Str. 3, 72076 Tuebingen, Germany

³ Nuclear Medicine and Clinical Molecular Imaging, Department of Radiology, Eberhard Karls University, Otfried-Mueller-Str. 14, 72076 Tuebingen, Germany

Abbreviations

SMS	Simultaneous multi-slice
STD	Standard
HASTE	Half Fourier acquisition single shot turbo spin echo
PSMA	Prostate-specific membrane antigen
SD	Standard deviation
CI	Confidence interval
TR	Repetition time

Introduction

Diffusion-weighted imaging (DWI) has become an essential part of the imaging of many oncological diseases [1]. It is able

to sensitively measure differences in diffusivity of water molecules and is therefore a valuable tool in detecting and characterizing various malignant lesions [2]. Cancer therapy can cause cell swelling or apoptosis which influences water diffusivity [3]. Thus, it has been shown that DWI may be helpful in the evaluation of therapy response [4]. DWI is technically demanding, and was first established in neuroimaging [5]. Further developments were necessary to transfer DWI to regions outside the brain so that it could be introduced into the daily routine of diagnostic imaging of individual organs [6, 7]. The introduction of the background body signal suppression technique [8] allowed DWI to be applied to whole-body examinations with acceptable acquisition times and image quality. However, DWI is still one of the most time-consuming sequences in whole-body protocols, hampering its broad clinical application.

The simultaneous excitation and acquisition of multiple slices (SMS) is one possible approach to reducing examination times. This technique was introduced in the late 1980s [9, 10], and is based on different sensitivities of multicoil arrays for separation of multiple slices. However, low sensitivity in separating closely spaced slices for a long time hindered its widespread application. More recently, advances such as the adaptation of parallel imaging technology [11] and the introduction of the “controlled aliasing in parallel imaging results in higher acceleration” (CAIPIRINHA) technique [12] and its modified version for the echoplanar imaging readout [13], has enabled today’s application of DWI-SMS in whole-body imaging [14, 15]. Being a functional imaging technique, DWI is often combined with or compared to positron emission tomography (PET) for oncological imaging [16–19]. For several years it has been possible to acquire PET and MRI simultaneously [20]. This has enabled the acquisition of multiple tissue parameters derived from PET and MRI at the same time with very good alignment [21] and has also opened up new technical possibilities such as using the MR information for motion correction of PET images [22–24]. However, with still rather long whole-body PET/MRI scan times, patient comfort and therefore also patient compliance are markedly reduced [25, 26].

Thus, the aim of this study was to compare image quality, lesion conspicuity and apparent diffusion coefficient (ADC) values in tumorous lesions and organs obtained using DWI-SMS with those obtained using standard DWI (DWI-STD) for multiparametric whole-body PET/MRI examination in oncological patients.

Materials and methods

This prospective study was approved by the local ethics committee. Written informed consent was obtained from all volunteers and patients regarding the examination and the scientific evaluation of their data.

MRI protocol

All examinations were performed on a fully integrated 3-T PET/MRI scanner (Biograph mMR; Siemens Healthineers, Erlangen, Germany). The specifications and performance of the MR component of the Biograph mMR system used are comparable to those of the Magnetom Verio system (Siemens Healthineers) [20]. The scan parameters for DWI-SMS (Multi-Band EPI package, release 13; Center for Magnetic Resonance Research, University of Minnesota, MN, USA) were adapted to the DWI-STD protocol used in our department for whole-body PET/MRI examinations (Table 1). In both techniques, an inversion recovery technique (spectral attenuated inversion recovery, SPAIR) was used for fat suppression. Two b -values were acquired: $b = 50 \text{ s/mm}^2$ and $b = 800 \text{ s/mm}^2$. All examinations were performed with the subject in free breathing. For anatomical correlation, a T2-weighted half Fourier acquisition single shot turbo spin echo (T2-HASTE) sequence with continuous table movement was acquired in all examinations with the subject in free breathing with the following parameters: echo time (TE) 76 ms, repetition time (TR) 1,200 ms, number of averages 1, flip angle 120° , and resolution $0.7 \times 0.7 \times 0.6 \text{ mm}$. Depending on the clinical indication, further sequences were performed in patients, but were not part of this study.

Phantom study

To assess the reliability of the quantification of diffusion restriction (ADC values) without subject-related artefacts, we performed a phantom study. Therefore, a dedicated sucrose DWI phantom was constructed to model different diffusivities (Fig. 1). Five tubes with a diameter of 25 mm were filled with sucrose solutions of different concentrations (0%, 10%, 20%, 30%, 40%) in distilled water and were placed in a cylindrical acrylic glass container filled with distilled water. DWI-STD and DWI-SMS sequences were performed using a multichannel head coil with the protocol parameters shown in Table 1. Each DWI sequence was applied twice successively with the same protocol parameters. All image datasets were transferred to a stand-alone workstation for offline postprocessing using MATLAB (MathWorks Inc, Natick, MA). Diffusion-weighted trace images I_{Trace} for two measured b -values ($b = 50$ and 800 s/mm^2) were calculated according to the following equation:

$$I_{\text{Trace}} = I_0 e^{-\text{ADC} \cdot b} = I_0 e^{-\frac{D_1 + D_2 + D_3}{3} \cdot b} = (I_1 \cdot I_2 \cdot I_3)^{\frac{1}{3}} \quad (1)$$

where I_1 , I_2 and I_3 are the measured diffusion-weighted images with three orthogonal gradient directions and D_1 , D_2 and D_3 are the corresponding diffusion coefficients. Their arithmetic mean results in the isotropic diffusion coefficient, namely ADC. The ADC maps were calculated from Eq. 1 using a log-linear fitting algorithm.

Table 1 Acquisition parameters of DWI-SMS and DWI-STD in patients/volunteers and in the phantom study (values in parentheses)

Parameter	DWI-SMS	DWI-STD
Image matrix	192 × 168 (128 × 112)	192 × 168 (128 × 112)
Slice thickness (mm)	5	5
Pixel size (mm ²)	2.2 × 2.2	2.2 × 2.2
No. of averages	3	3
<i>b</i> -values (s/mm ²)	50, 800	50, 800
Repetition time (ms)	3,000	6,000
Echo time (ms)	67 (59)	59 (59)
Bandwidth (Hz/pixel)	1,736 (1,698)	1,736 (1,698)
Coil combine mode	Sense1	Adaptive combine
Parallel acquisition mode / factor	GRAPPA / 3	GRAPPA / 2
Acquired slices (<i>n</i>)	34	34
Number of table positions	4–6	4–6
Scan time per table position (s)	84	140

GRAPPA generalized autocalibrating partially parallel acquisition, Sense sensitivity encoding

To minimize the impact of low-frequency spatially varying signal intensity, five rectangular regions of interest (ROIs), each of 21 pixels, were placed in each of the tubes to assess the ADC values. The ROIs were placed in the central region along the tube axis congruently in all reconstructed images. This was performed with the software Imagine (Imagine 2.0, Matlab Central File Exchange; MathWorks Inc., Natick, MA). The resulting ADC values in different sucrose solutions were calculated as the mean value over all five ROIs.

Volunteers

Between March 2016 and June 2016, ten healthy volunteers (aged 29 ± 9.3 years, five women) underwent PET/MRI examination in the supine position, arms positioned alongside the abdomen. All volunteers were examined from the cranial vertex to the thighs using head, body and spine multichannel coils. The MRI protocol was as described above.

The following evaluations were performed in the volunteers using the software *syngo.via* (*syngo.via* VA30; Siemens Healthineers, Erlangen, Germany).

ADC values and signal intensities in organs

For anatomical correlation, the T2-HASTE images in all volunteers were coregistered to the ADC maps and *b*50 images from DWI-SMS (ADC-SMS) and DWI-STD (ADC-STD). The ROIs were set congruently in all images in the white matter, the right liver lobe, the spleen, the kidney and the psoas muscle, avoiding image artefacts and organ borders.

Patients

Between May 2016 and September 2016, 20 patients (aged 62.3 ± 10.3 years, seven women) with the following

oncological diseases underwent a whole-body PET/MRI examination with both DWI-SMS and DWI-STD: melanoma (eight patients), lymphoma (four), neuroendocrine tumour (grade G2, three), prostate cancer (Gleason score 7b, one), lung cancer (one), breast cancer (one), renal cell carcinoma (one) and cancer of unknown primary (one). Inclusion criteria were a history of oncological disease with known or suspected metastases. Exclusion criteria were the typical contraindications for MRI, i.e. metal implants including pacemakers, and claustrophobia.

All patients undergoing PET/MRI were scanned from the cranial vertex to the thighs. Patients were positioned in the supine position, arms positioned alongside the abdomen and the MRI scan was performed as described above. ¹⁸F-FDG (average dose 315 MBq) was used as the PET tracer in patients with melanoma, lymphoma, lung cancer, breast cancer, renal cell carcinoma and cancer of unknown primary. The somatostatin receptor-specific radiotracer ⁶⁸Ga-DOMITATE (average dose 196 MBq) was used in patients with neuroendocrine tumours, and ⁶⁸Ga-PSMA (dose 172 MBq) was used in the patient with prostate cancer. PET images were reconstructed using the vendor's software and the following parameters: 3D ordered subsets expectation maximization algorithm, 21 subsets, two iterations, matrix size 256 × 256, voxel size 2.8 × 2.8 × 2mm³, 4-mm gaussian filter. For the vendor-provided attenuation correction, a segmentation-based attenuation map was generated with a T1-weighted spoiled gradient echo sequence in end-expiratory breath-hold with Dixon-based fat–water separation with the following parameters: TR 3.6 ms, TE1 1.23 ms, TE2 2.46 ms, flip angle 10°, pixel size 2.6 × 2.6 × 2.6 mm³. The attenuation map of each patient was carefully checked for artefacts.

Subjective image quality and artefacts

Subjective image quality was evaluated by two independent radiologists each with 5 years experience in DWI-MRI

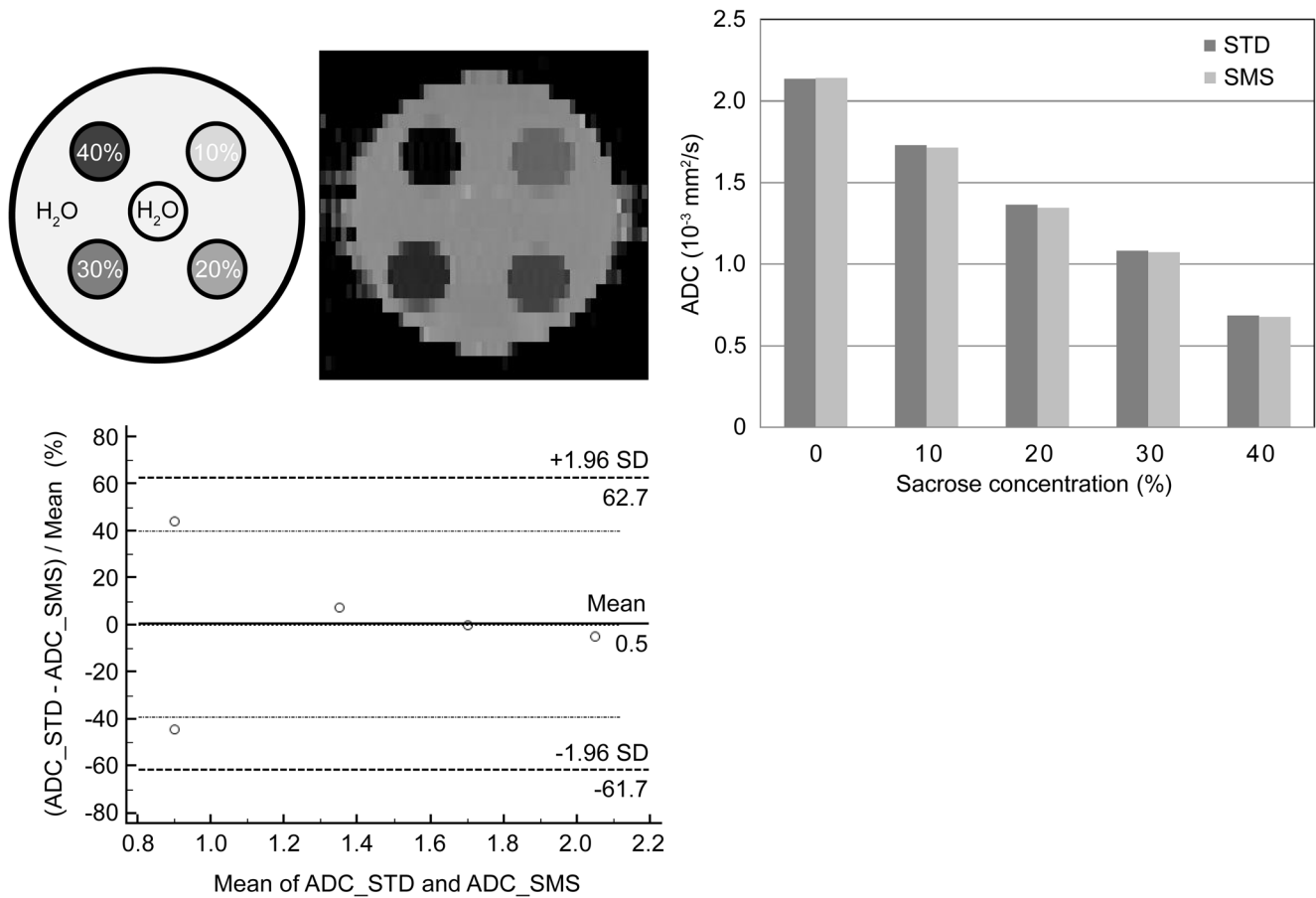


Fig. 1 Top left: DWI phantom and the corresponding ADC map (DWI-STD). Five tubes were filled with sucrose solutions of different concentration of sucrose solutions (0%, 10%, 20%, 30%, 40% in distilled water) and were placed in a cylindrical acrylic glass container filled with distilled water. Top right: ADC values acquired with different sucrose concentrations from ADC-STD and ADC-SMS maps (ADC values in $10^{-3} \text{ mm}^2/\text{s}$). Bottom: Bland-Altman plot of ADC values from the phantom measurements from the ADC-STD and ADC-SMS maps.

Differences between pairs of ADC values (expressed as percentages, y -axis) are plotted against the means of the pairs of ADC values (x -axis). The solid line indicates the mean absolute difference, the dashed black lines indicate $\pm 1.96 \times$ standard deviation, the dashed grey lines indicate 95% CI of the mean difference (limits of agreement), and the dotted grey line is the line of equality. Arithmetic mean 0.51% CI 38.9 to 40.0 $p=0.973$

(F.S. and J.T.) by reading the $b800$ images ($b800$ -SMS) and subsequently the ADC maps from the DWI-SMS in all patients, and 6 weeks later reading the $b800$ images ($b800$ -STD) and subsequently the ADC maps from the DWI-STD. The readings were performed in a blinded fashion. The readers were therefore not able to identify the respective imaging technique from any kind of image description. Subjective image quality was assessed in five different body regions which also corresponded to typical examination regions on PET: head, neck, thorax, abdomen and pelvis. This was performed using a five-point Likert scale relating to the delineation of organs and the overall diagnostic validity (5 excellent, 4 good, 3 satisfactory, 2 poor, and 1 nondiagnostic).

Image artefacts were evaluated in a consensus reading (F.S. and J.T.) in each body region separately and categorized into four different groups: (1) distortion artefacts, (2) ghosting

artefacts, (3) inhomogeneous fat saturation, and (4) other artefacts (caused by, for example, metal implants or interslice intensity variation). Artefacts were only assessed if they affected the investigated body region. The degree of observed artefacts was rated using a five-point Likert scale relating to the impact on the diagnostic validity of the image (5 low impact, 1 high impact).

Evaluation of tumorous lesions

All examinations were evaluated in a clinical setting in a consensus reading by a radiologist and a nuclear medicine physician, both with more than 10 years experience in hybrid imaging. Based on this report, two radiologists with 4 and 12 years experience in hybrid imaging (F.S. and C.S) evaluated the PET/MRI images from each patient in consensus, blinded to the respective DWI technique, and with the images opened

side-by-side: the PET images, the T2-HASTE images, the *b*800-SMS and the *b*800-STD images, and the ADC-SMS and ADC-STD maps.

In the first reading, the conspicuity of PET-positive tumorous lesions was evaluated on the *b*800-SMS and *b*800-STD images using a five-point Likert scale (5 very good, 1 not visible). Care was taken in the characterization of PET-positive tracer accumulations not to mistake possible inflammatory lesions for metastatic lesions. A maximum of ten lesions per organ were evaluated. For lymph nodes, a maximum of ten lymph nodes per body region (neck, thorax, abdomen, pelvis) were included. For peritoneal and pleural carcinomatosis, only circumscribed nodules were included. The longest diameter of a lesion was assessed in the axial plane in the T2-HASTE images. Cerebral metastases were not included in the evaluation.

In the second reading, the precision of ADC values of PET-positive tumorous lesions was evaluated. In order to only acquire possible deviations in ADC values derived from the respective acquisition technique, other influencing factors, such as partial volume effects and image artefacts, were eliminated. Therefore, only lesions with an axial diameter of >1 cm in the first reading were included in the evaluation of ADC values. The ADC values were assessed in a blinded fashion by drawing a free-hand intralesional ROI in the region of the lesion with the largest axial diameter on one of the ADC maps. The ROI was copied to the other ADC map; in individual cases, the ROI had to be relocated slightly but was not changed in size or shape. Care was taken to avoid blurred lesion borders on both ADC maps. Lesions were excluded from the evaluation if they were affected by artefacts on one of the ADC maps.

These evaluations were performed using the software *syngo.via* (*syngo.via* VA30; Siemens Healthineers).

Statistical analysis

Statistical analyses were performed using SPSS version 23.0 (IBM Corporation, Armonk, NY). The normality of distributions was tested using the Kolmogorov-Smirnov test. Likert scores and artefacts were compared using the Friedman test. For quantitative comparison of both sequences, ADC values were compared using Bland-Altman plots in percentages with limits of agreement ± 1.96 standard deviations (MedCalc for Windows, version 17.8.6; MedCalc Software, Ostend, Belgium). Equivalence was defined by the inclusion of the line of equality in the 95% confidence interval (CI) of the mean difference [27]. Analysis of variance with Bonferroni post hoc correction was performed if the comparisons showed significant differences. A *p* value <0.05 was considered statistically significant.

For interobserver agreement, kappa values were calculated with the following levels of agreement: 0.00 no agreement, 0.01–0.20 slight, 0.21–0.40 weak, 0.41–0.60 moderate, 0.61–0.80 strong, and 0.81–1.00 almost perfect [28]. Intraobserver agreement was calculated using the intraclass coefficient according to the method described by Fleiss [29] with the following levels of agreement: 0.00–0.40 poor, 0.041–0.75 fair to good, and 0.76–1.00 excellent.

Results

The DWI-STD and DWI-SMS scan times were 140 s and 84 s per table position, respectively, corresponding to a reduction in total scan time by 40%. The interobserver agreement in the evaluation of image quality was high (kappa 0.62 ± 0.03), and the intraobserver agreement in the evaluation of image quality was excellent (0.85, CI 0.823–0.875).

Phantom study

The results of the phantom study are shown in Fig. 1. Overall, the ADC values from the two techniques did not differ significantly (arithmetic mean 0.506%, CI –38.9 to 40.0%, *p* = 0.973 in the Bland-Altman plot). The highest difference in ADC values between the two techniques was found with the 20% sucrose solution (1.4%).

Volunteers

All examinations in volunteers were performed with five bed positions. The DWI scan times for the whole-body examinations were therefore 420 s for DWI-SMS and 700 s for DWI-STD. The ADC values in various organs obtained from the two techniques are given in Table 2. The ADC values in the liver and in the psoas muscle were significantly lower with DWI-SMS. Besides these regions, ADC values obtained with the two methods were considered equivalent. Bland-Altman plots of the body regions examined are shown in Fig. 2. Overall, a relative underestimation of ADC values with DWI-SMS was seen in tissues with low signal intensities in *b*50 images (Fig. 3).

Patients

The number of table positions varied between four and six, depending on the patient's height. The mean scan times were therefore 403 ± 44 s (range 336–504 s) for DWI-SMS and 672 ± 73 s (range 560–840 s) for DWI-STD.

Table 2 Mean ADC values and standard deviations ($\times 10^{-3}$ mm²/s) acquired in different body regions

Region	ADC-SMS	ADC-STD
White matter	0.8 ± 0.1	0.7 ± 0.1
Liver	0.9 ± 0.2	1.0 ± 0.1
Spleen	0.8 ± 0.1	0.8 ± 0.2
Kidney	1.9 ± 0.2	1.9 ± 0.2
Psoas muscle	1.3 ± 0.1	1.4 ± 0.1

Subjective image quality and artefacts

Subjective image quality ratings in the patient studies are shown in Table 3. No significant differences in subjective image quality ratings were found between the *b800*-SMS and *b800*-STD images. The subjective image quality ratings for the thoracic and abdominal regions were significantly lower on the ADC-SMS maps than on the ADC-STD maps.

More artefacts were found in the *b800*-SMS images than in the *b800*-STD images (Table 4). The diagnostic impact of artefacts in terms of the average of the artefact ratings did not differ significantly between the two

techniques (3.8 vs. 3.7, $p = 0.28$). In the corresponding ADC maps, artefacts were almost evenly distributed: 100 artefacts in the ADC-SMS maps and 104 artefacts in the ADC-STD maps (mean diagnostic impact values 3.8 vs. 3.8, $p = 0.28$).

Evaluation of tumorous lesions

PET-positive tumorous lesions were found in 19 of the 20 patients. In total, 116 lesions (diameter 2.0 ± 1.4 cm) were included in the first reading: 34 metastatic lymph nodes, 25 liver lesions, 16 bone lesions, 15 soft-tissue lesions, 13 lung lesions, 7 peritoneal lesions, 5 pleural lesions and 1 pancreatic lesion. The lesions were assigned to the body regions corresponding to those used in the evaluation of image quality (Table 5).

With both DWI techniques, lesion conspicuity was rated highest in the pelvis and lowest in the neck and thoracic region, as shown in the examples given in Fig. 4. Overall, lesion conspicuity did not differ significantly between the *b800*-SMS images and the *b800*-STD images. In the *b800*-STD images, 20 PET-positive lesions could not be delineated due to artefacts (Likert score 1): 5 in the neck region, 11 in the thoracic region, 2 in the

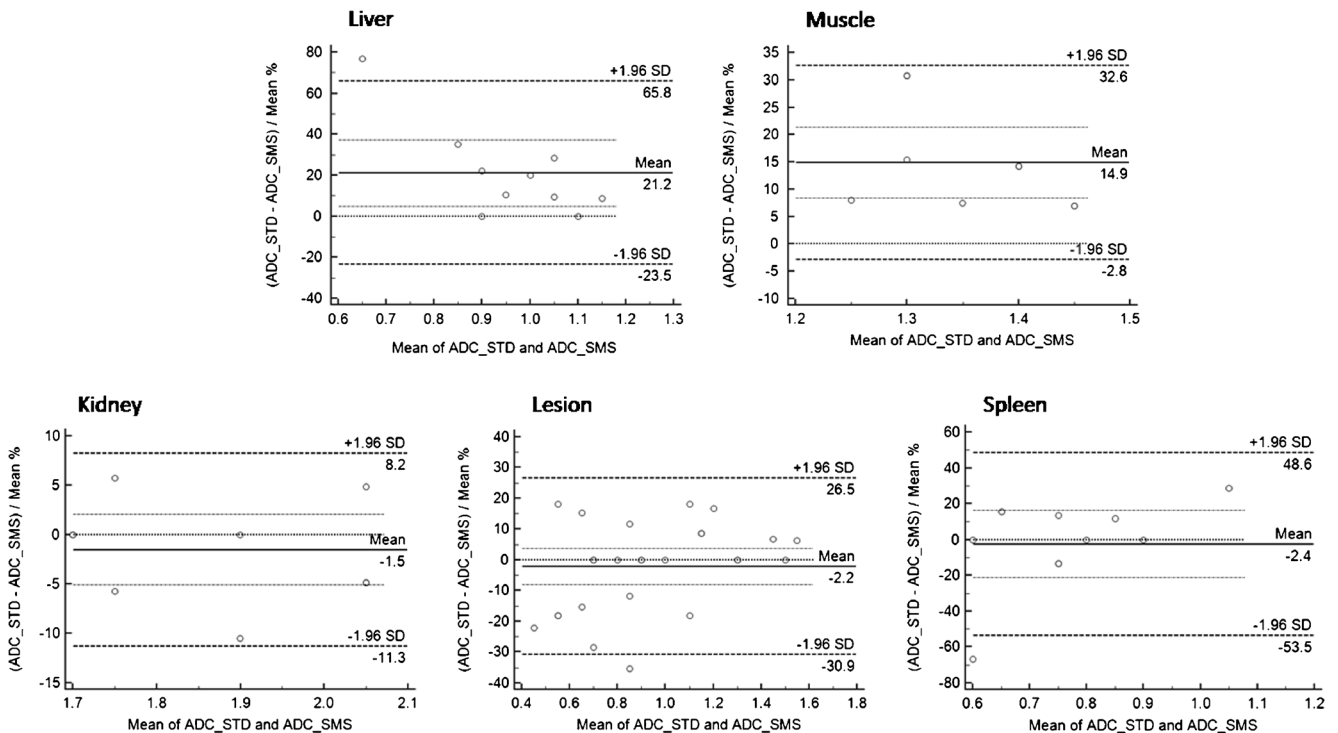


Fig. 2 Bland-Altman plots of ADC values measured from the ADC-STD and ADC-SMS maps (ADC values given in $\times 10^{-3}$ mm²/s) in various organs. Differences between pairs of ADC values (expressed as percentages, y-axis) are plotted against the means of the pairs of ADC values (x-axis). The solid line indicates the mean absolute difference, the dashed black lines indicate $\pm 1.96 \times$ standard deviation, the dashed grey lines

indicate 95% CI of the mean difference (limits of agreement), and the dotted grey line is the line of equality. For the liver and the psoas muscle, the line of equality does not lie within the interval of the 95% CI of the mean difference. For the kidney, the spleen and lesions, the line of equality lies within the interval of the 95% CI of the mean difference

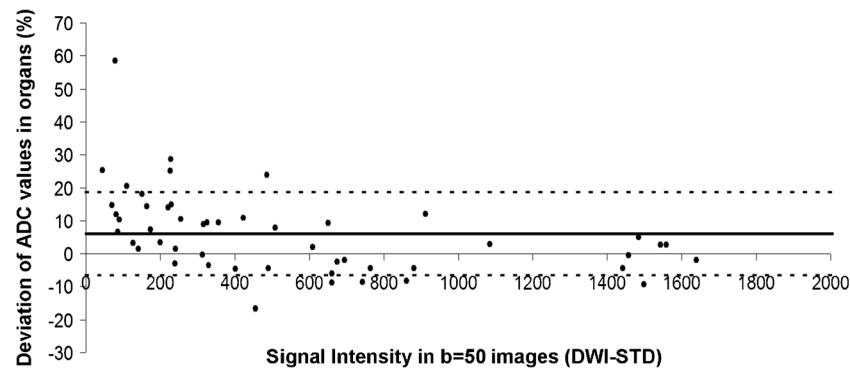


Fig. 3 Deviation of ADC values expressed as percentages [$100 \times (\text{ADC-STD} - \text{ADC-SMS})/\text{ADC-STD}$] and the respective signal intensity on the DWI-STD b50 images, together with the mean value (solid line) and

standard deviation (dashed lines). Lower signal intensities in the b50 image (i.e. in tissues with shorter T2 relaxation times) are associated with higher ADC value deviations in the SMS-accelerated sequence

abdomen (liver), and 3 in the upper thigh. Of these lesions, 6 were depicted in b800-SMS images. The average diameter of the missed lesions was 1.0 cm (range 0.5–2.0 cm). In the b800-SMS images, 16 PET-positive lesions could not be delineated due to artefacts: 3 in the neck region, 10 in the thoracic region, 2 in the abdomen (liver), and 1 in the pelvis. Of these lesions, 2 were depicted in the b800-STD images. The average diameter of these lesions was 1.3 cm (range 0.5–4.5 cm). Examples are given in Fig. 5.

For the evaluation of ADC values in lesions, 26 lesions (those with a diameter ≥ 1 cm in a region not affected by artefacts on DWI-SMS or DWI-STD) were evaluated, 9 metastatic lymph nodes, 5 bone lesions, 4 peritoneal lesions, 3 lung lesions, 2 liver lesions, 2 soft-tissue lesions and 1 pancreatic lesion. The average diameter of the lesions included in this evaluation was 3.3 cm (± 1.7 cm). Overall, no significant difference was found in the intralesional ADC values between the two DWI techniques (Fig. 6, Table 5).

Discussion

In this study, the DWI-SMS technique provided image quality in most body regions comparable to that provided by the DWI-STD technique, and reliable ADC values of tumorous

lesions for multiparametric whole-body PET/MRI examinations in oncological patients. The acquisition time with DWI-SMS as performed in this study (TR 3,000 ms) was 40% less than with DWI-STD (TR 6,000 ms).

A recent study by Kenkel et al. [30] showed that whole-body DWI-SMS at 3 T was technically feasible and showed promising results in eight volunteers and one patient. Nevertheless, there is still the need to investigate the diagnostic performance of whole-body DWI-SMS in oncological imaging in a larger patient cohort. Thus, we adapted a prototype DWI-SMS sequence for use with whole-body DWI, matching it to our whole-body DWI-STD protocol to perform a systematic comparison. The prototype SMS sequence used in this study has been proven to be technically feasible and has already shown promising results in liver imaging at 1.5 T [31, 32]. Although we applied a higher magnetic field strength, the DWI parameters (i.e. ADC) were expected to be unaffected by these changes [33]. Indeed, the ADC values measured were within the range of previously published values [30, 32, 34–36] and DWI-SMS provided reliable ADC values with no significant differences compared with DWI-STD in the phantom study, in most tissue types in the volunteer study and in the investigated tumorous lesions. However, ADC values measured with the SMS-accelerated sequence were found to be lower in tissues with a short T2 relaxation time (i.e. the liver) and/or a long T1 relaxation time (i.e. the psoas muscle) compared with those obtained with DWI-STD. A

Table 3 Mean values and standard deviations calculated from image quality rankings as rated by two independent radiologists for the b800 images and the ADC maps

Region	b800-SMS	b800-STD	<i>p</i> value	ADC-SMS	ADC-STD	<i>p</i> value
Head	4.1 \pm 0.4	3.9 \pm 0.3	>0.05	4.1 \pm 0.4	3.9 \pm 0.4	>0.05
Neck	3.4 \pm 0.7	3.1 \pm 0.6	>0.05	3.3 \pm 0.6	3.3 \pm 0.6	>0.05
Thorax	3.1 \pm 0.5	3.3 \pm 0.6	>0.05	2.8 \pm 0.5	3.4 \pm 0.7	0.03
Abdomen	3.3 \pm 0.7	3.6 \pm 0.8	>0.05	3.2 \pm 0.7	3.6 \pm 0.7	0.03
Pelvis	3.6 \pm 0.5	3.9 \pm 0.6	>0.05	3.8 \pm 0.5	3.9 \pm 0.7	>0.05

p values <0.05 were considered significant

Table 4 Overview of numbers and types of observed artefacts in the body regions examined and estimated impact on diagnostic validity in *b*800 images and ADC maps

Region	Artefact	DWI-SMS		DWI-STD	
		No. of artefacts	Impact	No. of artefacts	Impact
b800 images					
Head	Distortion	7	4.6	9	4.3
	Ghosting	2	4.0	0	/
Neck	Distortion	9	4.2	4	3.0
	Ghosting	13	3.5	17	3.2
	Fat saturation	5	4.2	1	4.0
	Other	6	3.0	6	3.0
Thorax	Distortion	2	4.0	0	/
	Ghosting	18	3.7	20	3.4
	Fat saturation	17	4.0	14	3.9
	Other	2	2.3	2	3.0
Abdomen	Distortion	2	4.0	0	/
	Ghosting	13	3.6	11	3.7
	Fat saturation	12	3.8	3	3.5
Pelvis	Distortion	13	4.1	6	4.7
	Ghosting	5	3.5	5	4.2
	Fat saturation	7	4.8	4	4.3
	Other	7	3.3	7	3.2
Sum / average diagnostic impact		140	3.8	109	3.7
ADC maps					
Head	Distortion	7	4.9	10	4.8
	Ghosting	3	4.8	2	4.3
Neck	Distortion	11	3.6	10	3.7
	Ghosting	12	3.4	10	3.3
	Fat saturation	0	/	1	4.0
	Other	2	3.5	2	4.0
Thorax	Distortion	1	5.0	4	4.3
	Ghosting	22	3.1	19	3.3
	Fat saturation	7	3.8	3	4.0
	Other	2	3.0	2	2.0
Abdomen	Distortion	1	4.0	4	4.4
	Ghosting	12	3.3	14	3.5
Pelvis	Distortion	6	4.7	12	4.6
	Ghosting	10	3.9	7	4.3
	Fat saturation	0	/	2	4.5
	Other	4	2.9	4	2.5
Sum/average diagnostic impact		100	3.8	106	3.8

^a Score 5 indicates low impact

possible explanation for this finding is the shorter TR with DWI-SMS (3,000 ms vs. 6,000 ms with DWI-STD) resulting in signal loss, an effect that has also been described by Kenkel et al. [30]. Thus, lower signal intensities in a tissue under study (e.g. hepatic tissue) due to a reduced TR (which is the case with SMS-DWI) automatically translates into lower ADC values. The relationship between ADC values and their signal intensities in the *b*50 images is given in Fig. 2.

In order to minimize DWI-SMS acquisition times, a TR as low as possible is chosen, resulting in only partial signal recovery causing a reduced signal in the acquired images [32]. Thus, generally lower signal intensity in *b*50 images (i.e. in tissue with a low T2) ultimately translates into lower ADC values and a larger deviation from ADC values measured with the standard sequence. However, as most malignant lesions possess T2 values higher than those of liver and muscle tissue,

Table 5 Mean values and standard deviations of lesion conspicuity as rated by two radiologists in consensus for the b800 images and mean ADC values with standard deviations for lesions with an axial diameter of >1 cm

	No. of lesions	b800-SMS	b800-STD	<i>p</i> value
Neck	7	3.0 ± 2.0	2.7 ± 2.1	0.32
Thorax	44	3.6 ± 1.7	3.4 ± 1.7	0.08
Abdomen	43	4.2 ± 1.3	4.4 ± 1.1	0.12
Pelvis	24	4.6 ± 1.0	4.5 ± 1.3	0.48
Overall	118	4.0 ± 1.5	3.9 ± 1.6	0.60
ADC values (x 10 ⁻³ mm ² /s)	26	0.9 ± 0.4	0.9 ± 0.4	

p values <0.05 were considered significant

^aScore 5 indicates very good lesion conspicuity

a significant deviation in lesion ADC values was not observed. A possible further explanation might be the divergent noise statistics or alteration in signal processing in the different sequences [31, 32]. The slightly reduced signal in DWI-SMS may account for the lower subjective image quality. This is of particular relevance in organs with low signal on DWI (e.g. the lung or the liver), and explains the lower subjective image quality found in the thoracic and abdominal regions with DWI-SMS. However, it needs to be stressed that DWI-STD also did not deliver optimal results in these body regions.

The b800-SMS sequence was more susceptible to artefacts than the b800-STD sequence. The source and strength of artefacts depends on various factors such as field homogeneity, gradient directions and the hardware installation [37], and their interpretation is complex. Yet, in spite of the discussed drawbacks of DWI-SMS, lesion conspicuity was preserved.

Contributing factors are certainly the fact that malignant lesions generally show higher signal intensity on T2-weighted images so that a pronounced signal loss is not expected. With both DWI-STD and DWI-SMS, the presence of artefacts reduced the conspicuity of individual lesions (Fig. 5).

There were some limitations to our study. First, the small number of patients allowed only a preliminary investigation of the use of DWI-SMS in multiparametric whole-body PET/MRI. Furthermore, only PET-positive lesions were evaluated in this analysis and set as the reference standard. PET-negative, yet possibly malignant, lesions were not included in the evaluation. The segmentation-based method used for attenuation correction can result in an underestimation of tracer uptake in regions with a high amount of bone and might therefore have affected the detectability of bone lesions [38]. A dedicated evaluation of brain metastases was beyond the

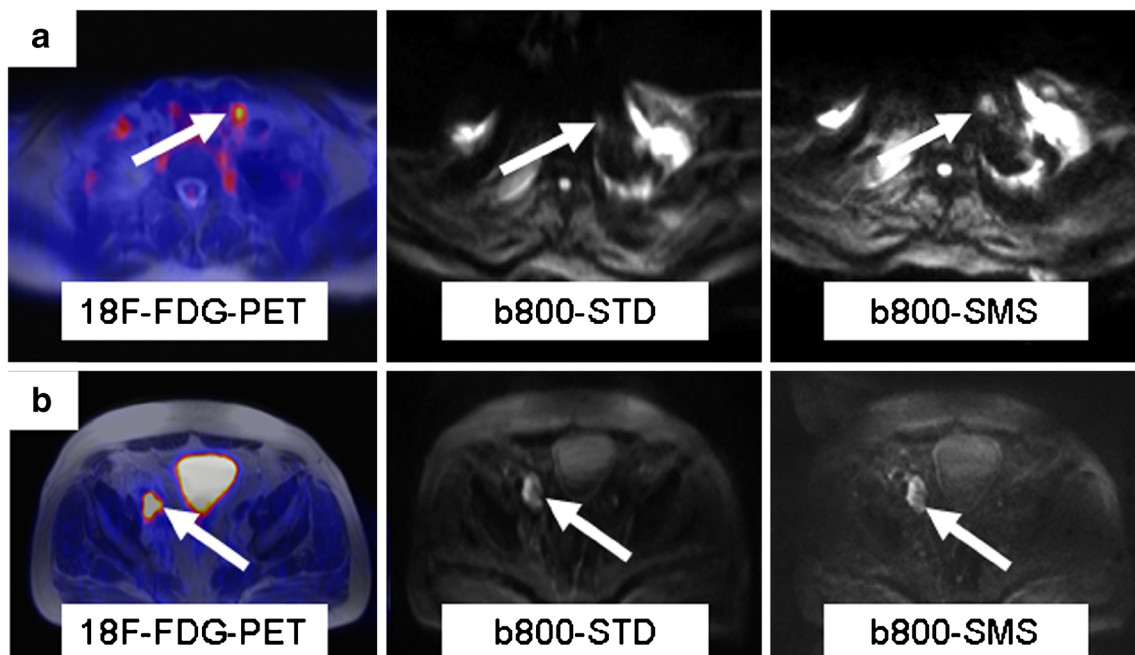


Fig. 4 Examples of lymph-node metastases in the upper thoracic region (a) and pelvis (b) positive on ¹⁸F-FDG PET/MRI. Due to artefacts, the lesion conspicuity in the upper thoracic/lower neck region (white arrows)

is impaired while the lesion conspicuity in the pelvis (white arrows) is good on both b800-STD and b800-SMS images

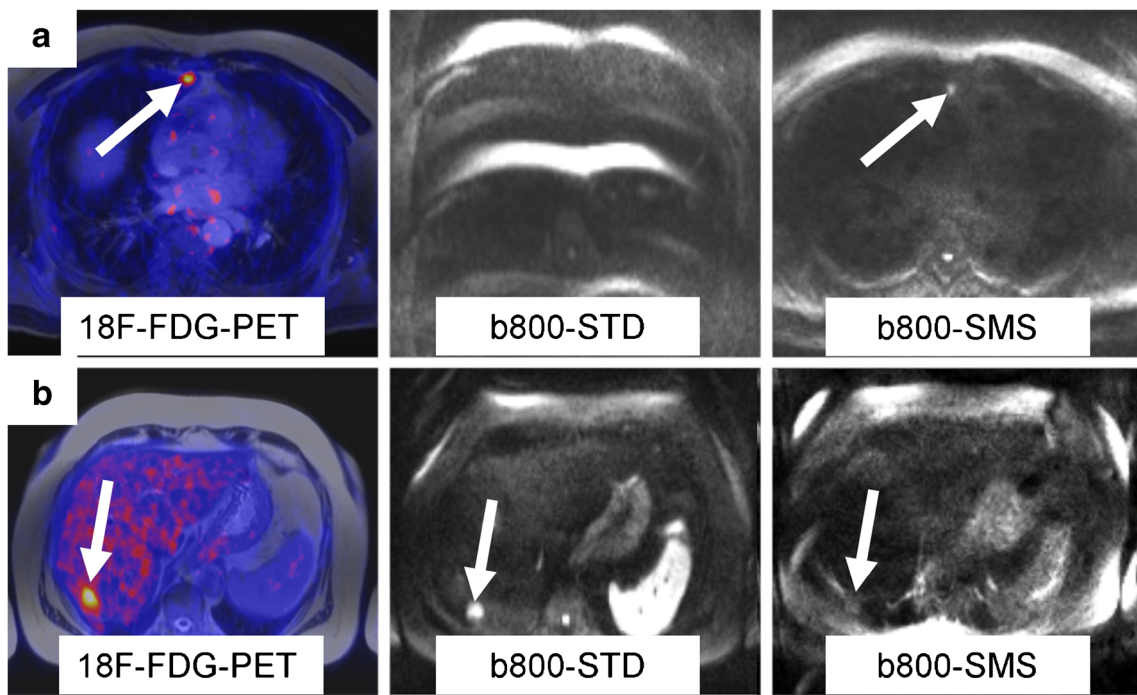


Fig. 5 Examples of impaired lesion conspicuity due to artefacts on both DWI-STD (a) and DWI-SMS (b). a A 64-year-old man with metastases from melanoma of the lung positive on ¹⁸F-FDG PET/MRI (white arrows) which is not visible on the DWI-STD image. b A 72-year-old

woman with metastases from melanoma of the liver positive on ¹⁸F-FDG PET/MRI (white arrows) which can hardly be delineated on the DWI-SMS image

scope of this work, but previous studies have demonstrated the usefulness of DWI-SMS techniques also in brain imaging [11, 39].

The sequence parameters for DWI-SMS were adapted to our DWI-STD. Thus, when applying DWI-SMS only, further optimization of parameters including *b*-values, number of averages, voxel size and slice thickness, is possible. Radiologists were blinded in the reading of the diffusion-weighted images but with time and with increasing experience, the differences between DWI-STD and DWI-SMS images became obvious, especially as the DWI-SMS images were presented first. However, the authors tried to minimize this effect by choosing a subsequent evaluation scheme. Moreover, the conspicuity of PET-positive metastases was evaluated in a consensus reading

which hampered the evaluation of interrater agreement. Finally, we did not obtain test–retest ADC values (as performed, for example in a previous study [40]) which might have given an indication of the repeatability of SMS-DWI and STD-DWI.

In conclusion, DWI-SMS seems to provide reliable lesion conspicuity and consistent ADC values of PET-positive tumorous lesions. Therefore, although suffering from slightly reduced image quality in comparison with DWI-STD, especially in the thoracoabdominal region, DWI-SMS has the potential to distinctly reduce scan times in oncological patients undergoing multiparametric whole-body PET/MRI examinations. Studies with larger numbers of patients should be encouraged to confirm our results.

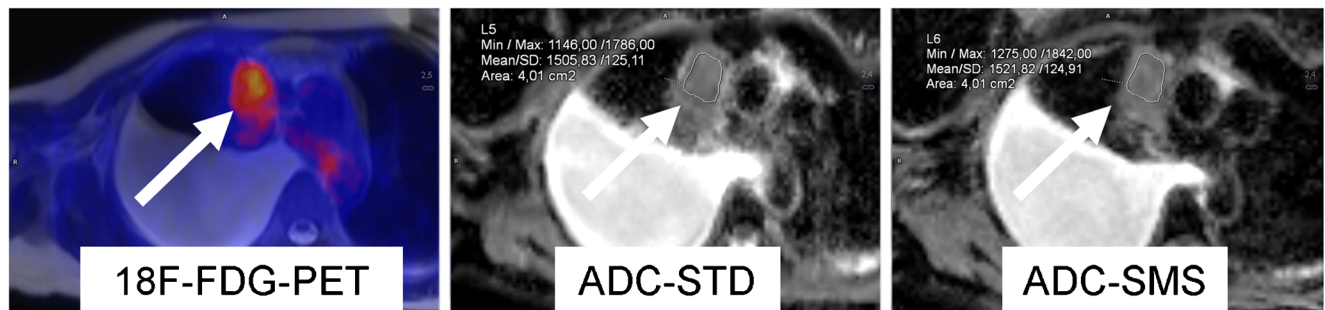


Fig. 6 A 48-year-old woman with breast cancer and lymph-node metastases in the mediastinum positive on ¹⁸F-FDG PET/MRI (white arrows). Note the good correlation between the mean ADC values (ADC-STD $1.505 \times 10^{-3} \text{ mm}^2/\text{s}$, ADC-SMS $1.521 \times 10^{-3} \text{ mm}^2/\text{s}$) in this lesion.

Acknowledgements The authors thank the University of Minnesota Center for Magnetic Resonance Research for providing continuous support regarding the SMS sequence. The authors gratefully acknowledge the support of Dr. Christian Wuerslin, Stanford, Radiological Sciences Laboratory, in kindly sharing the MATLAB postprocessing software. The authors thank Holger Schmidt, PhD, Siemens Healthineers GmbH, for kindly supporting the revision of the manuscript.

Compliance with ethical standards

Guarantor The scientific guarantor of this publication is Petros Martirosian.

Conflict of interest The authors of this manuscript declare no relationships with any companies whose products or services may be related to the subject matter of the article.

Funding The authors state that this work did not receive any funding.

Statistics and biometry No complex statistical methods were necessary for this paper.

Ethical approval Institutional Review Board approval was obtained.

Informed consent Written informed consent was obtained from all patients.

Methodology

- prospective
- experimental
- performed at one institution

References

1. Padhani AR, Koh D-M, Collins DJ (2011) Whole-body diffusion-weighted MR imaging in cancer: current status and research directions. *Radiology* 261:700–718
2. Holzapfel K, Reiser-Erkan C, Fingerle AA et al (2011) Comparison of diffusion-weighted MR imaging and multidetector-row CT in the detection of liver metastases in patients operated for pancreatic cancer. *Abdom Imaging* 36:179–184
3. Moffat BA, Chenevert TL, Lawrence TS et al (2005) Functional diffusion map: a noninvasive MRI biomarker for early stratification of clinical brain tumor response. *Proc Natl Acad Sci U S A* 102:5524–5529
4. Padhani AR, Koh DM (2011) Diffusion MR imaging for monitoring of treatment response. *Magn Reson Imaging Clin N Am* 19:181–209
5. Moseley ME, Cohen Y, Mintorovitch J et al (1990) Early detection of regional cerebral ischemia in cats: comparison of diffusion- and T2-weighted MRI and spectroscopy. *Magn Reson Med* 14:330–346
6. Yoshikawa T, Kawamitsu H, Mitchell DG et al (2006) ADC measurement of abdominal organs and lesions using parallel imaging technique. *AJR Am J Roentgenol* 187:1521–1530
7. Ichikawa T, Haradome H, Hachiya J, Nitatori T, Araki T (1998) Diffusion-weighted MR imaging with a single-shot echoplanar sequence: detection and characterization of focal hepatic lesions. *AJR Am J Roentgenol* 170:397–402
8. Takahara T, Imai Y, Yamashita T, Yasuda S, Nasu S, Van Cauteren M (2004) Diffusion weighted whole body imaging with background body signal suppression (DWIBS): technical improvement using free breathing, STIR and high resolution 3D display. *Radiat Med* 22:275–282
9. Müller S (1988) Multifrequency selective rf pulses for multislice MR imaging. *Magn Reson Med* 6:364–371
10. Souza SP, Szumowski J, Dumoulin CL et al (1988) SIMA: simultaneous multislice acquisition of MR images by Hadamard-encoded excitation. *J Comput Assist Tomogr* 12:1026–1030
11. Moeller S, Yacoub E, Olman CA et al (2010) Multiband multislice GE-EPI at 7 tesla, with 16-fold acceleration using partial parallel imaging with application to high spatial and temporal whole-brain fMRI. *Magn Reson Med* 63:1144–1153
12. Breuer FA, Blaimer M, Heidemann RM et al (2005) Controlled aliasing in parallel imaging results in higher acceleration (CAIPIRINHA) for multi-slice imaging. *Magn Reson Med* 53:684–691
13. Xu J, Moeller S, Auerbach EJ et al (2013) Evaluation of slice accelerations using multiband echo planar imaging at 3 T. *Neuroimage* 83:991–1001
14. Auerbach EJ, Xu J, Yacoub E, Moeller S, Ugurbil K (2013) Multiband accelerated spin-echo echo planar imaging with reduced peak RF power using time-shifted RF pulses. *Magn Reson Med* 69:1261–1267
15. Setsompop K, Cohen-Adad J, Gagoski BA et al (2012) Improving diffusion MRI using simultaneous multi-slice echo planar imaging. *Neuroimage* 63:569–580
16. Taouli B, Beer AJ, Chenevert T et al (2016) Diffusion-weighted imaging outside the brain: Consensus statement from an ISMRM-sponsored workshop. *J Magn Reson Imaging* 44:521–540
17. Kwee TC, Takahara T, Ochiai R et al (2010) Complementary roles of whole-body diffusion-weighted MRI and 18F-FDG PET: the state of the art and potential applications. *J Nucl Med* 51:1549–1558
18. Mayerhoefer ME, Karanikas G, Kletter K et al (2014) Evaluation of diffusion-weighted MRI for pretherapeutic assessment and staging of lymphoma: results of a prospective study in 140 patients. *Clin Cancer Res* 20:2984–2993
19. Preda L, Conte G, Bonello L et al (2016) Combining standardized uptake value of FDG-PET and apparent diffusion coefficient of DW-MRI improves risk stratification in head and neck squamous cell carcinoma. *Eur Radiol* 26:4432–4441
20. Delso G, Furst S, Jakoby B et al (2011) Performance measurements of the Siemens mMR integrated whole-body PET/MR scanner. *J Nucl Med* 52:1914–1922
21. Brendle CB, Schmidt H, Fleischer S, Braeuning UH, Pfannenber CA, Schwenzer NF (2013) Simultaneously acquired MR/PET images compared with sequential MR/PET and PET/CT: alignment quality. *Radiology* 268:190–199
22. Kustner T, Wurslin C, Schwartz M et al (2017) Self-navigated 4D cartesian imaging of periodic motion in the body trunk using partial k-space compressed sensing. *Magn Reson Med* 78:632–644
23. Fayad H, Schmidt H, Kustner T, Visvikis D (2017) 4-Dimensional MRI and attenuation map generation in PET/MRI with 4-dimensional PET-derived deformation matrices: study of feasibility for lung cancer applications. *J Nucl Med* 58:833–839
24. Dikaios N, Izquierdo-Garcia D, Graves MJ, Mani V, Fayad ZA, Fryer TD (2012) MRI-based motion correction of thoracic PET: initial comparison of acquisition protocols and correction strategies suitable for simultaneous PET/MRI systems. *Eur Radiol* 22:439–446
25. Guckel B, Gatidis S, Enck P et al (2015) Patient comfort during positron emission tomography/magnetic resonance and positron emission tomography/computed tomography examinations: subjective assessments with visual analog scales. *Invest Radiol* 50:726–732

26. Aghighi M, Pisani LJ, Sun Z et al (2016) Speeding up PET/MR for cancer staging of children and young adults. *Eur Radiol* 26:4239–4248
27. Giavarina D (2015) Understanding Bland Altman analysis. *Biochem Med (Zagreb)* 25:141–151
28. Landis JR, Koch GG (1977) The measurement of observer agreement for categorical data. *Biometrics* 33:159–174
29. Fleiss JL (1999) Reliability of Measurement. *The Design and Analysis of Clinical Experiments*. John Wiley & Sons, Hoboken, pp 1–32
30. Kenkel D, Wurnig MC, Filli L et al (2016) Whole-body diffusion imaging applying simultaneous multi-slice excitation. *Rofo* 188: 381–388
31. Taron J, Martirosian P, Erb M et al (2016) Simultaneous multislice diffusion-weighted MRI of the liver: analysis of different breathing schemes in comparison to standard sequences. *J Magn Reson Imaging* 44:865–879
32. Taron J, Martirosian P, Schwenzer NF et al (2016) Scan time minimization in hepatic diffusion-weighted imaging: evaluation of the simultaneous multislice acceleration technique with different acceleration factors and gradient preparation schemes. *MAGMA* 29: 739–749
33. Padhani AR, Liu G, Mu-Koh D et al (2009) Diffusion-weighted magnetic resonance imaging as a cancer biomarker: consensus and recommendations. *Neoplasia* 11:102–125
34. Kenkel D, von Spiczak J, Wurnig MC et al (2016) Whole-body diffusion tensor imaging: a feasibility study. *J Comput Assist Tomogr* 40:183–188
35. Rosenkrantz AB, Geppert C, Kiritsy M, Feiweier T, Mossa DJ, Chandarana H (2015) Diffusion-weighted imaging of the liver: comparison of image quality between monopolar and bipolar acquisition schemes at 3T. *Abdom Imaging* 40:289–298
36. Filli L, Wurnig M, Nanz D, Luechinger R, Kenkel D, Boss A (2014) Whole-body diffusion kurtosis imaging: initial experience on non-Gaussian diffusion in various organs. *Invest Radiol* 49:773–778
37. Le Bihan D, Poupon C, Amadon A, Lethimonnier F (2006) Artifacts and pitfalls in diffusion MRI. *J Magn Reson Imaging* 24:478–488
38. Seith F, Gatidis S, Schmidt H et al (2016) Comparison of positron emission tomography quantification using magnetic resonance- and computed tomography-based attenuation correction in physiological tissues and lesions: a whole-body positron emission tomography/magnetic resonance study in 66 patients. *Invest Radiol* 51:66–71
39. Feinberg DA, Moeller S, Smith SM et al (2010) Multiplexed echo planar imaging for sub-second whole brain fMRI and fast diffusion imaging. *PLoS One* 5:e15710
40. Weller A, Papoutsaki MV, Waterton JC et al (2017) Diffusion-weighted (DW) MRI in lung cancers: ADC test-retest repeatability. *Eur Radiol*. <https://doi.org/10.1007/s00330-017-4828-6>